LAWRENCE
LIVERMORE
NATIONAL
LABORATORY

LLNL-JRNL-763286

Design Considerations for Three-Dimensional Betavoltaics

J. W. Murphy, L. F. Voss, C. D. Frye, Q. Shao, K. Kazkaz, M. A. Stoyer, R. A. Henderson, R. J. Nikolic

November 30, 2018

AIP Advances

Disclaimer

This document was prepared as an account of work sponsored by an agency of the United States government. Neither the United States government nor Lawrence Livermore National Security, LLC, nor any of their employees makes any warranty, expressed or implied, or assumes any legal liability or responsibility for the accuracy, completeness, or usefulness of any information, apparatus, product, or process disclosed, or represents that its use would not infringe privately owned rights. Reference herein to any specific commercial product, process, or service by trade name, trademark, manufacturer, or otherwise does not necessarily constitute or imply its endorsement, recommendation, or favoring by the United States government or Lawrence Livermore National Security, LLC. The views and opinions of authors expressed herein do not necessarily state or reflect those of the United States government or Lawrence Livermore National Security, LLC, and shall not be used for advertising or product endorsement purposes.

Design considerations for three-dimensional betavoltaics

John W. Murphy*, Lars F. Voss, Clint D. Frye, Qinghui Shao, Kareem Kazkaz, Mark A. Stoyer, Roger A. Henderson, Rebecca J. Nikolic

Lawrence Livermore National Laboratory, 7000 East Ave, Livermore, CA 95440, USA

* murphy70@llnl.gov

Keywords: radioisotope battery, nuclear battery, betavoltaic

1. Abstract

Betavoltaic devices are suitable for delivering low-power over periods of years. Typically, their power density is on the order of nano to micro-Watts per cubic centimeter. In this work we evaluate the potential for using high-aspect ratio three-dimensional semiconductor structures to enhance the power and efficiency of these devices. The Monte Carlo transport code MCNP6 is used to provide realistic estimates of the theoretical levels of charge generation, which is in turn used to make predictions about the power output from three-dimensional betavoltaics. The focus of this work is on silicon and promethium-147, but other semiconductors and radioisotopes are considered as well. In the case of silicon diodes with three-dimensional features that are comparable to what is commercially available we estimate that power densities in the range of 20-25 mW/cm^3 can be achieved at efficiencies of 2.9-5.8% when coupled with promethium-147 oxide.

2. Introduction

Betavoltaic devices – power producing devices that operate via the direct generation of charge by ionization in a semiconductor from impinging beta decay particles – are a class of radioisotope or nuclear batteries that have been a subject of interest since the early 1950s [1,2]. For an overarching review of nuclear batteries see the 2014 paper by Prelas *et al*. [3]. Betavoltaics are desirable because they can potentially offer a high power conversion efficiency as compared to other radioisotope driven power sources such as radioisotope thermoelectric generators (RTGs), particularly for small-volume and relatively low activity devices, as the efficiency of RTGs is dependent on the temperature difference achievable [4].

In traditional betavoltaics the total power output and efficiency is limited due to the co-planar structure of the beta source and the semiconductor diode and the limited range of the beta particles in the source itself, which limits the thickness of the radioisotope source due to self-shielding – *i.e.*, the beta particles depositing their kinetic energy in the radioisotope source material rather than in the desired active region of the semiconductor. These directional and self-shielding effects have traditionally constrained the efficiency of semiconductor betavoltaics to 1-2% [5]. More recently efficiencies of 5-18% have been demonstrated with 4H-silicon carbide (4H-SiC), however these have been co-planar devices with power outputs only on the order of a micro-Watt or less [6–8]. Three-dimensionally structured devices have

been proposed in the past, specifically utilizing promethium-147 as the radioisotope and silicon as the semiconductor [9,10]. There are several recent works evaluating the optimal design of betavoltaic devices, but they are primarily focused on a co-planar structure [11–13]. In this work we provide a rigorous treatment of how to predict ultimate power density and efficiency for what we see as practically realizable three-dimensional structures. A comparison of optimal feature sizes for various radioisotopes and semiconductors in terms of achievable output power densities and efficiencies is presented. We will discuss the choice of semiconductor, radioisotope, and provide insights on predicting the optimal geometry for a three-dimensionally structured betavoltaic device for a given semiconductor and radioisotope.

3. Methodology

A schematic showing a comparison between a traditional co-planar betavoltaic device and a three-dimensionally structured device is shown in Figure 1.

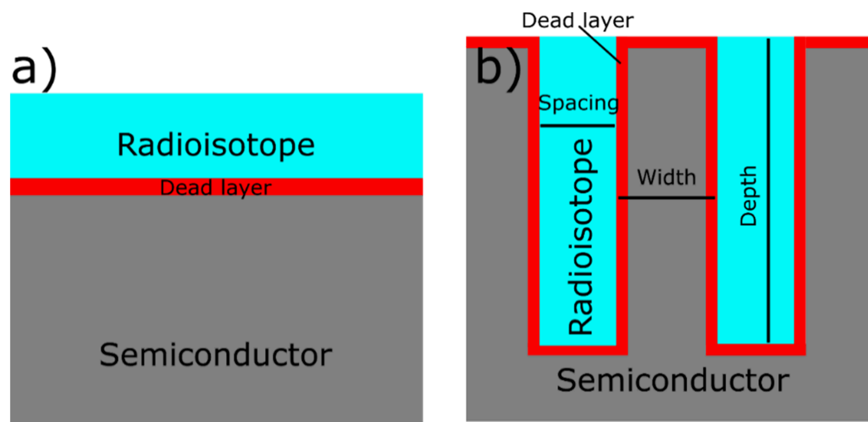

Figure 1- Comparison of (a) traditional co-planar betavoltaic with (b) three-dimensionally structured betavoltaic device.

The overall losses in efficiency of a betavoltaic device has been described by Wacharasindhu *et al.* [5] as shown in eq. 1:

$$L_{total} = L_d + L_a + L_{ex} + L_i \quad \text{(eq. 1)}$$

Where L_{total} is the total loss, L_d are directional losses due to beta particles emitted in a direction that does not travel towards the active semiconductor region of the device, L_a are absorption losses that account for kinetic energy of beta particles lost in the radioisotope source itself, L_{ex} are external losses due to beta particles passing through a "dead layer" such as a metallic electrode or highly doped semiconductor layer, and L_i are losses internal due to incomplete charge collection in the active region of the semiconductor. The use of three-dimensionally structured semiconductors can primarily mitigate directional losses, L_d, and absorption losses in the radioisotope source material, L_a. A similar effect may be achieved by stacking many very thin, discrete semiconductor diodes with thin layers of radioisotope material sandwiched between them, however we regard manufacturing the devices as a monolithic structure as a more practical fabrication process.

MCNP6 v1.0 was used to simulate the transport of charged particles through the source and semiconductor material, as well as to tally the energy deposited in the semiconductor by the beta particles. For all geometries a device area of 1×1 cm^2 was used and at least 5×10^5 particle histories were simulated resulting in a relative error for all tallies of less than 0.1. Python scripts were used to generate the MCNP6 input files, submit them to MCNP, and then parse and compile data from the output files. Electrons were transported until their energy decreased to 100 eV, and using the EPRDATA12 library data for transport for energies below 1 keV [14]. The three-dimensional, high-aspect ratio features were 400 µm deep in a 500 µm thick substrate. Charge generation in the semiconductor region was evaluated using an F8 pulse height tally and converting energy to e-h pairs using the ionization energies shown in Table 1 - Selected semicondcutor properties. From the charge generated on a per particle basis, a short-circuit current was calculated based on the activity of the source material and assuming charge collection was 100% efficient in the semiconductor regions being considered. Based on the estimated short-circuit current, I_{SC}, an open-circuit voltage, V_{OC}, was calculated as shown in eq. 2, based on reference [15]:

$$V_{OC} = n * \frac{kT}{q} \ln(\frac{I_{SC}}{I_0}) \qquad \text{(eq. 2)}$$

Where n is the ideality factor of the diode, k is Boltzmann's constant, T is temperature, taken as 300 K, q is the fundamental charge in Coulombs, I_{SC} is the short-circuit current, and I_0 is the saturation current of the device. The ideality factor, n, was taken as 2, which is typical for p-i-n structured diodes, and values for I_0 are shown in Table 1. The saturation current values for Si and 4H-SiC in Table 1 were taken from experimentally extracted curves from three-dimensionally structured devices. In theory these will depend on both the volume of the depleted semiconductor region as well as the total area of the p-n junction, but for this work an effective value was used where the area is normalized to the aerial chip size as the relative contributions of these two components are not known. From the open-circuit voltage an electrical fill-factor was calculated using eq. 3 as described in reference [16]:

$$FF = \frac{v_{oc} - \ln(v_{oc} + 0.72)}{v_{oc} + 1} \qquad \text{(eq.3)}$$

Where v_{oc} is the reduced open-circuit voltage, which is the open-circuit voltage normalized to the thermal voltage, nkT/q. Power density was calculated as $V_{OC} \cdot I_{SC} \cdot FF$ normalized by the combined volume of the full semiconductor wafer thickness including the ridges and base as well as the radioisotope source. Finally, an efficiency was calculated by normalizing the predicted electrical power output by the total power produced by the radioisotope source, which was calculated as the average beta particle energy expressed in Joules multiplied by the decay rate of the total quantity of radioactive source material in the device, as shown in eq. 4:

$$\eta = \frac{V_{OC} \cdot I_{SC} \cdot FF}{E_{avg} \cdot A} \qquad \text{(eq.4)}$$

Where the numerator represents the predicted electrical power output, and in the denominator E_{avg} is the mean energy of the beta particles produced by the source in Joules, and A represents the total

activity in Becquerel or decay rate per second of the radioisotope source material in the device. Calculations were made assuming a temperature of 300 K.

4. Design Considerations

The choice of semiconductor, radioisotope, and geometry are dictated by numerous factors, including device operational lifetime, cost restrictions, and manufacturability. In this section an overview of considerations with regards to semiconductor, geometry, and radioisotope will be discussed.

5.1 Choice of Semiconductor

The choice of semiconductor plays a significant role in the performance of a betavoltaic device. The bandgap is a critical factor that will determine the device leakage or saturation current and in turn the open-circuit voltage of the device. Related to the bandgap is the ionization energy required to form an electron-hole pair in the semiconductor. The bandgap type, whether direct or indirect is also important as indirect bandgap materials tend to have significantly longer minority carrier diffusion lengths, meaning the energy absorbing region of the semiconductor may not need to be fully depleted during operation. Another consideration is the maturity of fabrication and processing technologies to form three-dimensional structures in the semiconductor. Selected semiconductor properties for silicon, 4H-SiC, and gallium nitride are shown in Table 1 [17–19].

The saturation current densities shown in Table 1 were experimentally measured from three-dimensionally structured devices – for silicon from a ridged diode procured from Radiation Detection Technologies, Inc., and for4H-SiC from a device fabricated at LLNL. In theory the saturation current density will change with the geometry of the devices as the exact geometry will vary the loss terms due to the ratio of minority carrier injection, depletion layer recombination, and tunneling [20], but the contribution of these terms is not precisely known, so we chose to use these experimental values for calculating the open-circuit voltage in all simulations.

Table 1 - Selected semicondcutor properties; values taken from references [17] *for Si,* [18] *for 4H-SiC, and* [19] *for GaN (Saturation currents are taken from measurements on Radiation Detection Technologies, Inc. Si and Lawrence Livermore National Laboratory SiC three-dimensionally structured diodes).*

Semiconductor	Bandgap (eV)	Bandgap type	Ionization energy (eV)	Saturation current density (A/cm^2)
Silicon	1.12	Indirect	3.61	4.7×10^{-8}
4H-Silicon Carbide	3.27	Indirect	7.28	5×10^{-23}
Gallium Nitride	3.45	Direct	~10	-

5.1.1 Silicon

Silicon is not ideal from the stand-point of betavoltaics due to its relatively low bandgap. Although a small bandgap allows for more charge carriers to be generated due to lower ionization energy, it also leads to higher leakage or saturation currents and thus lower overall power density and efficiency due to lower operating voltage [20]. However, its ease of processing, wide availability of electronic grade substrates with thicknesses up to a millimeter or greater, and relatively low cost make it suitable for

consideration. Processing advantages include the ability to wet etch high-aspect ratio three-dimensional structures and form a conformal junction around them, in which the highly doped region conforms and wraps-around the high-aspect ratio intrinsic semiconductor region, which passivates the surface as well as improving charge collection [21,22]. It also has a relatively high damage threshold from electron bombardment, ~300 keV [23–25], making it less susceptible to damage from the beta sources under consideration in this paper.

5.1.2 4H-Silicon Carbide

4H-SiC has a wide, indirect bandgap which makes it well-suited for betavoltaic devices, and has also recently been demonstrated as a functional betavoltaic in a flat co-planar geometry with high charge collection efficiency using a tritium-based source [6,8]. However, it is more difficult to fabricate high-aspect ratio three-dimensional structures as dry-etching proceeds fairly slowly and may introduce deep-level defects [26], and conformal doping of such structures is not well-developed, although recent technology may make this feasible [27]. It is also susceptible to damage from electron bombardment at energies of 100-120 keV [28], although it does not suffer damage from betas ~60 keV [29].

5.1.3 Gallium Nitride and Other III-V Semiconductors

Gallium nitride (GaN) is a semiconductor with a bandgap of 3.45 eV. It is desirable due to its large bandgap energy, however it is a direct bandgap material, so the active region of the device would need to be fully depleted or have a very fine feature size on the order of one micron, as the diffusion length of minority carriers in GaN will be on the order of 0.5-1 µm even for homoepitaxially grown material [30]. The manufacture of high-aspect ratio three-dimensional structures has been demonstrated using both top-down [31–33] and bottom-up [34,35] approaches. GaN is also reported to be very radiation hard in general [36], as well as having a damage threshold from electron bombardment of greater than 400 keV [37].

Gallium arsenide [38] and indium gallium phosphide [39] have been investigated for use in betavoltaic devices, however they suffer from many of the same processing issues as GaN and 4H-SiC with respect to formation of high-aspect ratio structures, conformal doping, and limited minority carrier lifetime, while also having a smaller bandgap, so they are not as theoretically efficient [20].

5.2 Choice of 3-Dimensional Geometry

The three geometries considered in this work, ridges, holes, and pillars, are shown schematically in Figure 2.

5.2.1 Ridges

Ridges or fins are the simplest geometry to fabricate for Si as they can be formed by wet etching a 110 wafer in a potassium hydroxide or tetramethylammonium hydroxide solution [21,40], which simplifies fabrication due to the avoidance of surface damage from dry etching that can produce recombination centers increasing leakage current and reducing charge collection efficiency [21]. Ridged structures are described by the width of the semiconductor ridge and the width of the trench/spacing between ridges.

5.2.2 Holes

Holes are formed by etching cylindrical voids into the semiconductor. This geometry has been demonstrated for use in semiconductor-based neutron detectors [41]. This geometry is defined by the diameter of the holes and the size of the "pixel" containing each hole, where the pixels are arranged in a hexagonally close-packed arrangement as viewed from the top-down.

5.2.3 Pillars

Pillars in the semiconductor material are formed by etching the semiconductor material into cylindrical pillars and are described by the diameter of the pillar and the size of the "pixel" containing each pillar. They have been demonstrated in solar cells [42] as well as neutron detectors [43–45]. They are the inverse of the hole geometry. Pillar geometries (*i.e.*, nanowires or microwires) are the most-studied architecture in terms of a bottom-up growth approach [46]. Pillar structures, and likely hole structures as well, could potentially be formed by wet etching, at least in silicon, via electrochemical or metal-assisted chemical etching, but it is not certain whether features as deep as 400 µm would be possible [47].

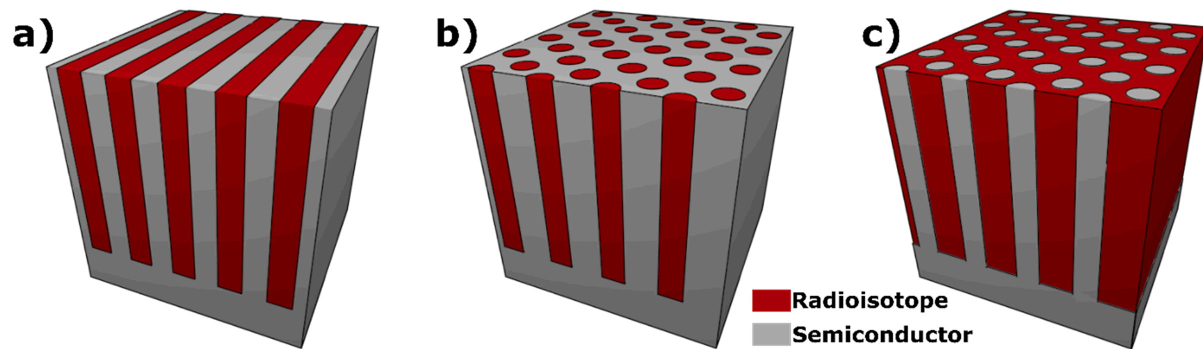

Figure 2 - Schematic of three-dimensional geometries shown with radioisotope material shown as red and semiconductor as grey: (a) ridges, (b) holes, and (c) pillars.

5.3 Choice of Radioisotope

Table 2 shows the properties of several selected radioisotope materials, including half-life, average energy, and mass density, as well as their calculated theoretical maximum power density, which is calculated as shown in eq. 5:

$$P_{dens} = A_{sp} \cdot E_{avg} \cdot \rho \cdot e \qquad \text{(eq.5)}$$

where P_{dens} is the power density, A_{sp} is the specific activity (related to half-life), E_{avg} is the average beta decay particle kinetic energy, ρ is the mass density, and e is the fundamental electric charge. For radioisotope pairs in which the daughter nuclide decays many times faster than the parent, ^{106}Ru/Rh, ^{90}Sr/Y, and ^{32}Si/P, a specific activity of two times the parent nuclide was used and an average of the two mean beta energies to calculate the theoretical maximum power density. The power density versus half-life and mean energy are shown graphically in Figure 3 [48–50].

Table 2 - Properties of selected radioisotope materials – half-life and energy data taken from reference [48]*, density information for titanium tritide and nickel taken from* [49] *and promethium oxide density from* [50]*.*

Radioisotope	Formula	Half-life (y)	Mean beta (keV)	Beta end-point (keV)	Density (g/cm^3)	Max power density (mW/cm^3)
Sulfur-36	S	0.24	48.7	167	2.07	25519.2
Ruthenium-106/Rhodium-106	Ru/Rh	1.022	10.0/1410	39.4/3540	12.45	345563.5
Promethium-147 oxide	Pm_2O_3	2.6234	61.93	225	6.85	2004.1
Krypton-85 (500 PSI)	Kr	10.756	250	687	0.116	67.3
Tritium (500 PSI)	H_2	12.32	5.68	18.6	0.0028	0.9
Titanium tritide	$TiH_{1.4}$	12.32	5.68	18.6	3.75	97.9
Strontium-90/Yttrium-90	Sr/Y	28.79	196/931	546/2280	2.54	4687.2
Nickel-63	Ni	100.1	17.42	66.9	8.90	52.1
Silicon-32/Phosphorous-32	Si/P	132	68.6/695	225/1710	2.33	8.93
Carbon-14	C	5700	49.45	156	2.26	2.88

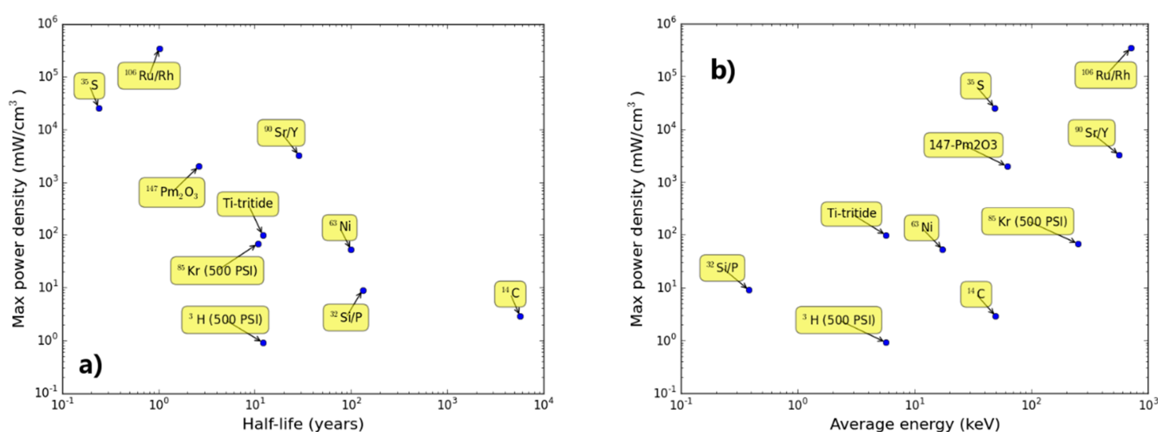

Figure 3- Maximum theoretical power density for various radioisotopes plotted versus (a) half-life and (b) mean beta energy.

5.3.1 Titanium tritide

Tritium, in the form of titanium tritide, is an attractive material for betavoltaics because titanium forms a stable hydride that can achieve relatively high tritium concentrations, approximately 1.4-1.5 tritium atoms per titanium [51]. It is also the most abundant and lowest-cost per Curie of the radioisotopes considered here by a factor of 1000x, as of 2012 [52]. Its half-life of approximately 12 years is well-suited for betavoltaics. There are no issues with gamma emission either by tritium or impurities, as the tritium can be purified by distillation [53], and there are no problematic decay chain products, as the only decay product is ^{3}He. The low average beta energy, 5.68 keV, is not ideal from the stand point of power generation because each beta will generate relatively few electron-hole pairs and will lose a significant amount of energy as it passes through electrodes or highly doped regions into the active semiconductor region, however it will make shielding the device straightforward and there is no concern about damaging the semiconductor due to high energy betas displacing atoms from the lattice. The low-energy of the beta particles also means that finer features will be necessary to achieve anything close to the maximum theoretical power density, as features larger than ~1 µm will result in very significant absorption losses, making very high aspect ratio device fabrication difficult to manufacture. Gaseous

tritium has also been explored, but due to its lower theoretical power density and the issues with handling and storing a radioactive gas, the tritide based materials are more attractive [52].

5.3.2 Nickel-63

Nickel-63 is attractive because it can be deposited by electroless or electro deposition for conformal coating of high-aspect ratio semiconductor structures [54]. Similar to tritium, there are no problematic decay-chain products or impurities, and the relatively low-energy betas will not damage the semiconductor, but will necessitate fairly small features of several microns or less. However, nickel-63 is fairly expensive [52], and its long half-life of over 100 years makes it difficult to achieve high power densities.

4.3.3 Promethium-147 oxide

Promethium-147 oxide ($^{147}Pm_2O_3$) is an attractive material due to its high theoretical power density, twenty times greater than titanium tritide. The high energy of the beta particles, on average 62 keV but reaching up to ~220 keV [48], is problematic for 4H-SiC due to deep levels generated by atomic displacement of carbon atoms [28], however Si [23–25] and GaN [37] will not likely suffer due to atomic displacement damage. The relatively high energy of the beta particles and long range (~20 µm) also allows for larger features without suffering severe degradation in power output and efficiency due to the longer range of the betas in solid materials, on the order of 10-20 µm, making fabrication of the devices more straightforward. One concern is that there will be impurity content of promethium-146, as promethium-146 emits gamma rays with energies up to 747 keV, making shielding a concern as well as potential displacement damage to any semiconductor from Compton scattered electrons or photoelectrons [55].

5.2.4 Other radioisotope source materials

Other possible beta sources are unattractive due to an energy spectrum that significantly exceeds the damage threshold, too long or short of a half-life, or unwanted decay products from other reaction pathways or daughter nuclei such as alphas, gammas, or higher energy beta emission. $^{90}Sr/Y$, $^{32}Si/P$, and $^{106}Ru/Rh$ are considered as single radioisotope sources, as yttrium-90, phosphorous-32, and rhuthenium-106 are daughter nuclides with much shorter half-life, on the order of seconds to hours, so they will quickly reach an equilibrium concentration with the parent nuclide. $^{90}Sr/Y$ [56] and krypton-85 [57] have been given consideration in the past for direct conversion betavoltaic devices, however, due to the fact that both of these radioisotope materials emit betas with energies that will damage any semiconductor by atomic displacement, they are not suitable for long-term device operation. Silicon-32 and Ruthenium-106 suffer from a similar issue as they have short-lived daughter isotopes that emit high energy betas. Carbon-14 is attractive in terms of beta energy and no undesirable decay products, but the very long half-life limits the achievable power density. ^{36}S has been recently used to demonstrate novel liquid-semiconductor betavoltaic devices[5,58], but the very short half-life makes a device with lifetime on the order of years impractical.

5. Results and Discussion

In order to study the design space, we evaluated radioisotope materials and semiconductors from the choices mentioned previously using MCNP6 for the various sample geometries. For all the simulations the substrate size is kept at 1×1 cm^2, the substrate thickness is 500 µm, and the depth of the features (ridges, holes, or pillars) is kept at 400 µm.

6.1 Ridge width and spacing with Si semiconductor for selected radioisotopes

Initially, we evaluate the performance of silicon ridged structures filled with each of the three radioisotope materials under consideration, titanium tritide, nickel-63, and $^{147}Pm_2O_3$, in terms of their power density and efficiency as a function of both the ridge width and spacing, shown schematically in Figure 1b. In these simulations the space between the ridges is filled with radioisotope material at its maximum theoretical density. The results of these simulations are shown in Figure 4. These devices are also "ideal" because there is no dead layer at the semiconductor/radioisotope interface, as previously discussed and illustrated in Figure 1. The beta spectrum for each source material was exported from reference [48] and used in MCNP6, which includes relativistic effects for higher energy beta particles.

As can be seen in the power density plots in Figure 4 the $^{147}Pm_2O_3$ device is generally one to two orders of magnitude higher than the nickel-63 and titanium tritide devices. The $^{147}Pm_2O_3$ device also allows for larger features in terms of both the ridge width and spacing, 10-20 µm, while maintaining a relatively high power density due to the longer range of the higher energy beta particles that it emits. The $^{147}Pm_2O_3$ simulations were done over a range of 1-30 µm for the ridge width and spacing, while the $Ti^3H_{1.4}$ and ^{63}Ni simulations were done over a range of 0.5 to 2.2 or 5 µm, because beyond that the power density and efficiency drop to very low values. The general shape of the surface plots is similar for the three radioisotopes with the maximum power density occurring at the combination of the smallest ridge width and spacing. This combination allows for the most radioisotope per cm^2 to fit in the closest proximity to the most semiconductor material. As can be seen in Figure 4 on the efficiency plots, the efficiency is also highest for the smallest ridge spacings, as source self-shielding is minimized. However, the power density is only maximized when the source self-shielding is minimized (small ridge spacings) *and* the amount of radioisotope per chip is maximized (*i.e.*, small ridge width, or high spacing:width ratio).

Nickel-63, and to an even greater degree titanium tritide, require very fine features to come close to their maximum power density, on the order of 1 µm. The fabrication and filling of features close to 1 µm with high aspect ratio has been demonstrated experimentally with copper in silicon (holes 3-80 µm wide and 45-160 µm deep) [59],and could likely be adapted for nickel, but filling with titanium tritide is less certain. As a comparison, features on the order of 10-20 µm with a depth of 400+ µm, conformal doping, and filling with LiF nanopowder have been commercially demonstrated by Kansas State University and Radiation Detection Technologies, Inc. [21].

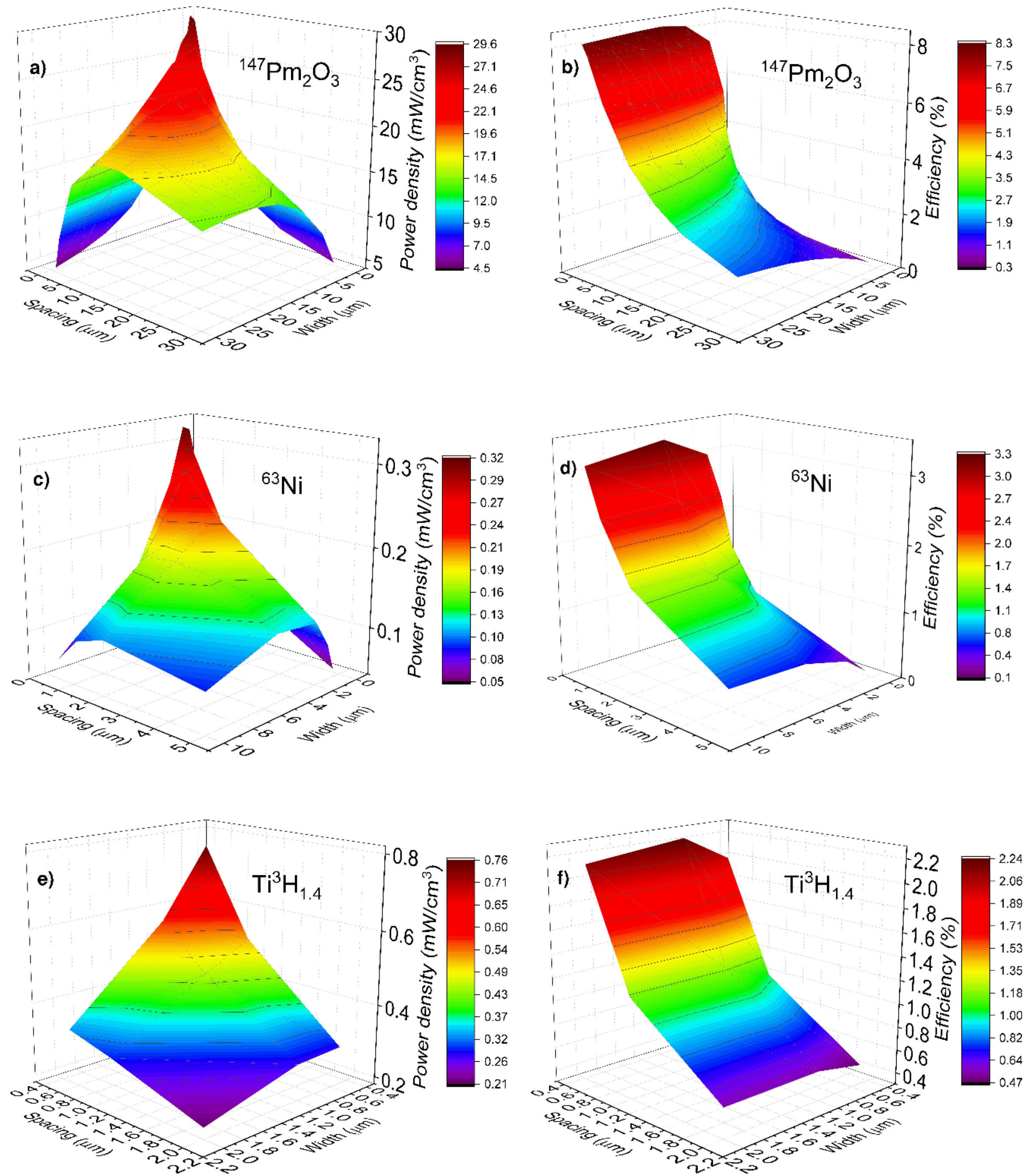

Figure 4 - Power density and efficiency of ideal ridged devices filled with (a, b) $^{147}Pm_2O_3$, (c, d) ^{63}Ni, (e, f), $Ti^3H_{1.4}$.

6.2 Effect of p+/dead layer with Si and $^{147}Pm_2O_3$ versus Ni and tritium tritide for optimal geometry

The formation of a conformal junction for high aspect ratio semiconductor diodes is important for two reasons: (1) the highly doped conformal layer that forms the junction acts as a passivation layer to

mitigate surface recombination on the device's large surface area and reduce leakage current [21], and (2) a conformal junction lessens the requirement on the semiconductor's minority carrier diffusion length as the depletion region will extend down the length of the three-dimensional feature, so carriers will not have to diffuse to a junction that is located only at the top of the three-dimensional semiconductor structure. However, this highly doped layer that serves to form a conformal junction on the three-dimensional semiconductor structure will likely also effectively function as a "dead" layer, where charge that is generated by the beta particles is not collected due to the extremely short minority carrier lifetime in very highly doped semiconductors. For these reasons we evaluated the performance of the three radioisotope materials under consideration as a function of dead layer thickness. The geometry used was the ridged structure with ridge widths and spacings of 10 µm for the case of $^{147}Pm_2O_3$, ridge widths and spacings of 2 µm for the case of ^{63}Ni, and ridge widths and spacings of 1 µm for the case of titanium tritide. These feature sizes were selected as they allow for mean energy beta particles to pass through the full spacing filled with radioisotope material, and they all produce approximately 70% of the maximum power density of the ideal case with no dead layer shown in Figure 4. The results are normalized to the case of no dead layer. A schematic of the geometry used for these simulations with a highly doped dead layer wrapping around the top, sides, and bottom of the semiconductor ridges where no charge collection will occur is shown in Figure 1b.

As can be seen in Figure 5, titanium tritide suffers the most from the introduction of a dead layer, because of the low energy of the beta particles emitted – for the case of a 200 nm dead layer more than half of the theoretical power is lost in the conformal dead layer. Nickel-63 fairs significantly better, losing only about 30% of possible power output with the introduction of a 200 nm dead layer, and promethium suffers only an approximately 5% loss for the case of a 200 nm dead layer.

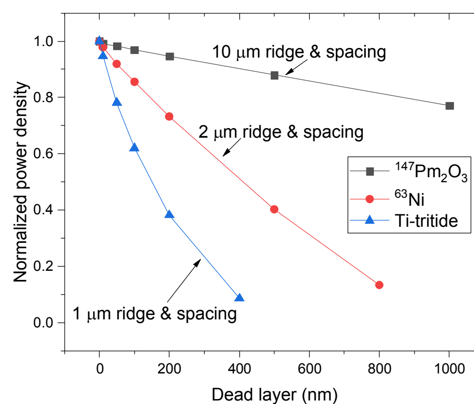

Figure 5 - Normalized power density versus dead layer thickness for 10 x 10 µm Si ridges filled with $^{147}Pm_2O_3$, 2 x 2 µm Si ridges filled with ^{63}Ni, and 1 x 1 µm Si ridges filled with titanium tritide.

6.3 Comparison of ridges vs. holes vs. pillars for Pm and Si

In this section we evaluate the performance of ridged versus hole versus pillar geometries for silicon and promethium-based devices, each of which is shown schematically in Figure 2. This was done by setting a "pixel size" of 20 µm and varying the "feature size" within that pitch. For the ridged simulations this

amounts to the sum of the ridge width and spacing being held constant at 20 µm. For the hole and the pillar simulations this was implemented as 20 µm "pixels" arranged in a hexagonal close space packing, as shown in Figure 2. In the center of each pixel either a hole filled with radioisotope or a pillar of semiconductor with a diameter that defined the "feature size" was used. The pitch was kept constant at 20 µm as this is a feature size that has been demonstrated commercially for very high aspect ratio silicon devices [60], and it is fairly close to the CSDA range of an average energy beta from a promethium-147 decay in silicon, which is around 30 µm.

Based on these simulations, the results of which are shown in Figure 6, a slightly higher power density can be achieved with a greater efficiency for the pillar devices compared to the ridged devices: the maximum power density for the pillars is 25.6 mW/cm^3 which occurs at an 18 µm pillar diameter/feature size with an efficiency of 4.36%, while the maximum power density for the ridged simulations is 23.9 mW/cm^3 which occurs at a 8 µm ridge width/feature size with an efficiency of 3.7%. Based on these simulations pillars are able to deliver 7% more power than the optimal ridge geometry for this case of a 20 µm "pitch" of silicon feature filled with fully dense Pm_2O_3 but are able to do so with a nearly 18% increase in efficiency. This is a significant improvement; however, pillar fabrication would necessitate dry-etching, which would significantly complicate the fabrication by making low leakage currents more difficult to achieve for a large-area and high-aspect ratio device. It would also complicate the process of making electrical contact to the each pillar in the array, while ridged and hole geometries have a continuous top surface to make contact with.

The hole geometry does not perform as well as the ridged geometry for the best scenario considered – the maximum power density is 23.9 mW/cm^3 for a 15 µm diameter hole, which is the same maximum power density as the 8 µm wide ridge, however the efficiency for the 15 µm diameter hole is only 3.37%, or nearly 9% less than the 8 µm ridged structure. The reason for this is that packing the radioisotope into a circular feature tends to maximize self-shielding in the radioisotope source material. This is why the pillar geometry leads to the best efficiency at its maximum power density, as it maximizes both the interfacial area of the source/semiconductor interface and the total radioisotope source volume.

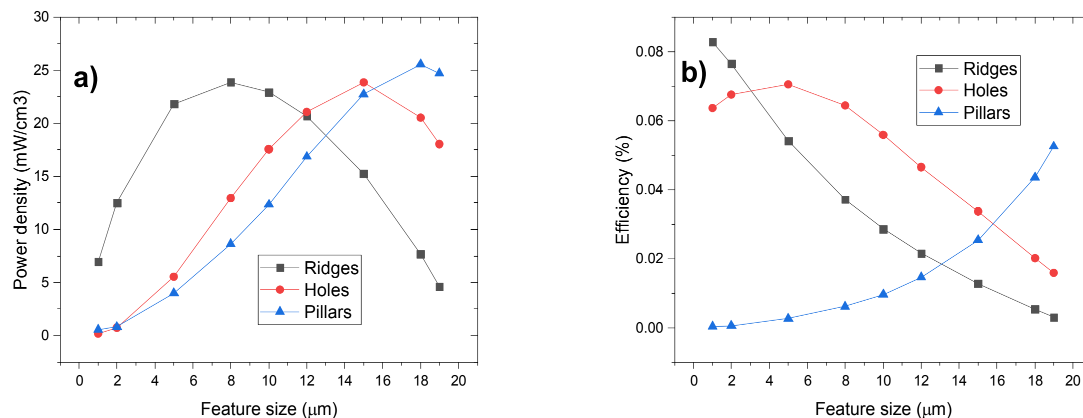

Figure 6 - Comparison of the (a) power density and (b) efficiency of ridge, hole, and pillar geometries for Pm_2O_3 and Si based device with feature sizes ranging from 1-19 µm in a 20 µm pitch.

6.4 Comparison of Si vs. 4H-SiC with $^{147}Pm_2O_3$ Fill

The performance of a ridged structure of SiC filled with fully dense Pm_2O_3 and no dead layer is shown in Figure 7. This demonstrates how much greater performance can be achieved with 4H-SiC compared to silicon. Whereas for silicon, as shown in Figure 4a and b, the maximum power density and efficiency for very small ridge widths and spacings are ~30 mW/cm^3 and 8%, respectively, the maximum power density and efficiency for 4H-SiC are over 85 mW/cm^3 and 24%, respectively, as shown in Figure 7. This is because although 4H-SiC requires approximately twice as much energy to produce an electron-hole pair compared to silicon (see Table 1), the output voltage of the 4H-SiC device will be approximately five to six times greater than the Si device due to the larger bandgap (and thus much smaller saturation current), which produces an approximate tripling of performance in terms of both power density and efficiency. This figure clearly illustrates why wide bandgap semiconductors are so attractive for betavoltaic applications. However, it should be noted that a promethium based source will displace carbon atoms from the lattice of a 4H-SiC based betavoltaic [28], resulting in degraded performance over time.

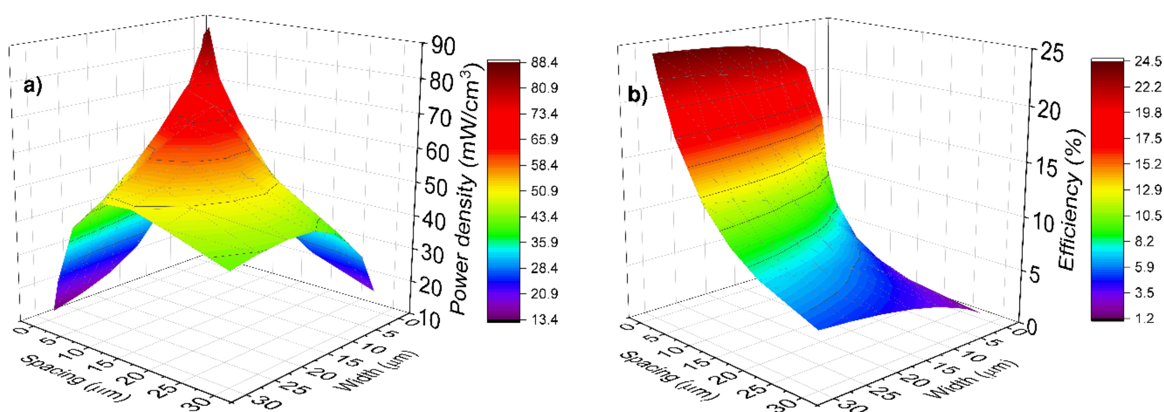

Figure 7 - Ideal power density (a) and efficiency (b) of SiC ridged structures with Pm.

6. Conclusions

We have evaluated three-dimensional semiconductor structures, focusing on silicon, coupled with three likely candidate radioisotope materials and provided realistic estimates of the attainable power density and efficiency as a function of feature size. The effect of a “dead-layer” due to a conformal wrap-around junction was assessed for each of the three radioisotopes. Three different geometries were considered – ridges, holes, and pillars; slightly higher power densities and efficiencies can be achieved with the pillar and hole geometries, but would necessitate using dry etching techniques, while in silicon very high aspect ratio ridged structures can be achieved with wet etching, which avoids surface damage associated with dry etching. The potential for significantly higher power density and efficiency by replacing silicon with silicon carbide was also explored, which can theoretically increase power density and efficiency by more than a factor of nearly 3x, but at this point in time fabrication of these very high

aspect ratio semiconductor devices has only been commercially achieved in silicon. For a ridged silicon based with a ridge width and spacing of 10 µm, a depth of 400 µm, and a conformal wrap-around junction that results in a dead-layer of 200 nm filled with dense $^{147}Pm_2O_3$ we estimate that a power density of 21.7 mW/cm^3 could be achieved with an efficiency of 2.9%. If slightly finer features could be fabricated in silicon, such as a 5 µm ridge width with 2 µm spacing, still with a depth of 400 µm and a 200 nm conformal dead layer, then we estimate a dense fill of $^{147}Pm_2O_3$ could produce 24.1 mW/cm^3 at 5.8% efficiency. These numbers represent a significant improvement over the traditional co-planar geometry which is typically limited to power densities on the order of µW/cm^3.

Acknowledgments

This work was performed under the auspices of the U.S. Department of Energy by Lawrence Livermore National Laboratory under Contract DE-AC52-07NA27344, LLNL-JRNL-763286.

References

[1] Ehrenberg W, Lang C-S, West R. The Electron Voltaic Effect. Proc Phys Soc Sect A 1951;64:424. doi:10.1088/0370-1298/64/4/109.

[2] Rappaport P. The Electron-Voltaic Effect in p-n Junctions Induced by Beta-Particle Bombardment. Phys Rev 1954;93:246–7. doi:10.1103/PhysRev.93.246.2.

[3] Prelas MA, Weaver CL, Watermann ML, Lukosi ED, Schott RJ, Wisniewski DA. A review of nuclear batteries. Prog Nucl Energy 2014;75:117–48.

[4] Litz M. Isotope Beta-Battery Approaches for Long-Lived Sensors: Technology Review. 2014.

[5] Wacharasindhu T, Nullmeyer BR, Kwon JW, Robertson JD, Garnov AY. Mechanisms leading to losses in conventional betavoltaics and evolution: Utilizing composite semiconductor with infused radioisotope for efficiency improvement. J Microelectromechanical Syst 2014;23:56–65.

[6] Chandrashekhar MVS, Thomas CI, Li H, Spencer MG, Lal A. Demonstration of a 4H SiC betavoltaic cell. Appl Phys Lett 2006;88:33506.

[7] Eiting CJ, Krishnamoorthy V, Rodgers S, George T, Robertson JD, Brockman J. Demonstration of a radiation resistant, high efficiency SiC betavoltaic. Appl Phys Lett 2006;88:64101.

[8] Thomas C, Portnoff S, Spencer MG. High efficiency 4H-SiC betavoltaic power sources using tritium radioisotopes. Appl Phys Lett 2016;108:13505.

[9] Duggirala R, Tin S, Lal A. 3D silicon betavoltaics microfabricated using a self-aligned process for 5 milliwatt/cc average, 5 year lifetime microbatteries. Solid-State Sensors, Actuators Microsystems Conf. 2007. TRANSDUCERS 2007. Int., 2007, p. 279–82.

[10] Guo H, Yang H, Zhang Y. Betavoltaic microbatteries using porous silicon. Micro Electro Mech. Syst. 2007. MEMS. IEEE 20th Int. Conf., 2007, p. 867–70.

[11] Zhang K, Gui G, Pathak P, Seo J-H, Blanchard JP, Ma Z. Quantitative modeling of betavoltaic microbattery performance. Sensors Actuators A Phys 2016;240:131–7.

[12] Alam TR, Pierson MA, Prelas MA. Design Principles of Narrow and Wide Bandgap-Based Betavoltaic Batteries. IEEE Trans Electron Devices 2018;65:5518–24.

[13] Alam TR, Spencer MG, Prelas MA, Pierson MA. Design and optimization of radioisotope sources for betavoltaic batteries. Int J Energy Res 2018;42:2564–73.

[14] Goorley JT, James MR, Booth TE, Brown FB, Bull JS, Cox LJ, et al. MCNP6 User's Manual, Version 1.0. Los Alamos Natl Lab Los Alamos 2013.

[15] Schroder DK. Semiconductor material and device characterization. John Wiley & Sons; 2006.

[16] Green MA. Solar cell fill factors: General graph and empirical expressions. Solid State Electron 1981;24:788–9.

[17] Goulding FS, Landis DA. Signal processing for semiconductor detectors. IEEE Trans Nucl Sci 1982;29:1125–41.

[18] Chaudhuri SK, Zavalla KJ, Mandal KC. Experimental determination of electron-hole pair creation energy in 4H-SiC epitaxial layer: An absolute calibration approach. Appl Phys Lett 2013;102:31109.

[19] Litz M. Monte Carlo Evaluation of Tritium Beta Spectrum Energy Deposition in Gallium Nitride (GaN) Direct Energy Conversion Devices. 2014.

[20] Olsen LC. Review of betavoltaic energy conversion. 12th Sp. Photovolt. Res. Technol. Conf. (SPRAT 12), 1993.

[21] McGregor DS, Bellinger SL, Shultis JK. Present status of microstructured semiconductor neutron detectors. J Cryst Growth 2013;379:99–110.

[22] Huang KC, Dahal R, Lu JJQ, Weltz A, Danon Y, Bhat IB. Scalable large-area solid-state neutron detector with continuous p-n junction and extremely low leakage current. Nucl Instruments Methods Phys Res Sect A Accel Spectrometers, Detect Assoc Equip 2014;763:260–5. doi:10.1016/j.nima.2014.06.047.

[23] Summers GP, Burke EA, Shapiro P, Messenger SR, Walters RJ. Damage correlations in semiconductors exposed to gamma, electron and proton radiations. IEEE Trans Nucl Sci 1993;40:1372–9.

[24] Auret FD, Deenapanray PNK. Deep level transient spectroscopy of defects in high-energy light-particle irradiated Si. Crit Rev Solid State Mater Sci 2004;29:1–44.

[25] Lindström G. Radiation damage in silicon detectors. Nucl Instruments Methods Phys Res Sect A Accel Spectrometers, Detect Assoc Equip 2003;512:30–43.

[26] Kimoto T, Cooper JA. Fundamentals of Silicon Carbide Technology: Growth, Characterization, Devices and Applications. John Wiley & Sons; 2014.

[27] Tin C-C, Mendis S, Chew K, Atabaev I, Saliev T, Bakhranov E, et al. Oxide film assisted dopant diffusion in silicon carbide. Thin Solid Films 2010;518:e118--e120.

[28] Storasta L, Bergman JP, Janzén E, Henry A, Lu J. Deep levels created by low energy electron

irradiation in 4 H-SiC. J Appl Phys 2004;96:4909–15.

[29] Shao Q, Voss LF, Murphy JM, Frye CD, Henderson RA, Stoyer MA, et al. Accelerated aging in 4H-SiC as a betavoltaic semiconductors using an electron beam system. 2017.

[30] Collins KC, Armstrong AM, Allerman AA, Vizkelethy G, Van Deusen SB, Leonard F, et al. Proton irradiation effects on minority carrier diffusion length and defect introduction in homoepitaxial and heteroepitaxial n-GaN. J Appl Phys 2017;122:235705.

[31] Harrison SE, Voss LF, Torres AM, Frye CD, Shao Q, Nikolić RJ. Ultradeep electron cyclotron resonance plasma etching of GaN. J Vac Sci Technol A Vacuum, Surfaces, Film 2017;35:61303.

[32] Sun M, Zhang Y, Gao X, Palacios T. High-performance GaN vertical fin power transistors on bulk GaN substrates. IEEE Electron Device Lett 2017;38:509–12.

[33] Liu Z, Ishikawa K, Imamura M, Tsutsumi T, Kondo H, Oda O, et al. Temperature dependence on plasma-induced damage and chemical reactions in GaN etching processes using chlorine plasma. Jpn J Appl Phys 2018;57:06JD01.

[34] Hartmann J, Steib F, Zhou H, Ledig J, Fündling S, Albrecht F, et al. High aspect ratio GaN fin microstructures with nonpolar sidewalls by continuous mode metalorganic vapor phase epitaxy. Cryst Growth Des 2016;16:1458–62.

[35] Kumaresan V, Largeau L, Oehler F, Zhang H, Mauguin O, Glas F, et al. Self-induced growth of vertical GaN nanowires on silica. Nanotechnology 2016;27:135602.

[36] Pearton SJ, Ren F, Patrick E, Law ME, Polyakov AY. Ionizing radiation damage effects on GaN devices. ECS J Solid State Sci Technol 2016;5:Q35--Q60.

[37] Ionascut-Nedelcescu A, Carlone C, Houdayer A, Von Bardeleben HJ, Cantin J-L, Raymond S. Radiation hardness of gallium nitride. IEEE Trans Nucl Sci 2002;49:2733–8.

[38] Chen H, Jiang L, Chen X. Design optimization of GaAs betavoltaic batteries. J Phys D Appl Phys 2011;44:215303.

[39] Cress CD, Landi BJ, Raffaelle RP, Wilt DM. InGaP alpha voltaic batteries: synthesis, modeling, and radiation tolerance. J Appl Phys 2006;100:114519.

[40] Koirala M, Wu JW, Weltz A, Dahal R, Danon Y, Bhat I. Electrophoretic Deposition of 10B Nano/Micro Particles in Deep Silicon Trenches for the Fabrication of Solid State Thermal Neutron Detectors. Int J High Speed Electron Syst 2018;27:1840002.

[41] Huang KC, Dahal R, Lu JJQ, Danon Y, Bhat IB. High detection efficiency micro-structured solid-state neutron detector with extremely low leakage current fabricated with continuous p-n junction. Appl Phys Lett 2013;102:3–6. doi:10.1063/1.4802204.

[42] Kendrick CE, Redwing JM. Silicon Micro/Nanowire Solar Cells. Semicond. Semimetals, vol. 94, Elsevier; 2016, p. 185–225.

[43] Nikolic RJ, Conway AM, Reinhardt CE, Graff RT, Wang TF, Deo N, et al. 6 : 1 aspect ratio silicon pillar based thermal neutron detector filled with 10 B. Appl Phys Lett 2008;93:133502.

[44] Shao Q, Voss LF, Conway AM, Nikolic RJ, Dar MA, Cheung CL. High aspect ratio composite structures with 48.5% thermal neutron detection efficiency. Appl Phys Lett 2013;102:48–52. doi:10.1063/1.4792703.

[45] Nikolic RJ, Conway AM, Radev R, Shao Q, Voss L, Wang TF, et al. Nine element Si-based pillar structured thermal neutron detector. Hard X-Ray, Gamma-Ray, Neutron Detect Phys XII 2010;7805:78050O. doi:10.1117/12.862391.

[46] Zhang A, Zheng G, Lieber CM. Emergence of nanowires. Nanowires, Springer; 2016, p. 1–13.

[47] Elbersen R, Vijselaar W, Tiggelaar RM, Gardeniers H, Huskens J. Fabrication and Doping Methods for Silicon Nano-and Micropillar Arrays for Solar-Cell Applications: A Review. Adv Mater 2015;27:6781–96.

[48] Eckerman KF, Sjoreen AL. Radiological toolbox user's guide. United States Nuclear Regulatory Commission, Office of Nuclear Regulatory Research; 2013.

[49] Haynes WM. CRC Handbook of Chemistry and Physics 2016.

[50] Chikalla TD, McNeilly CE, Roberts FP. Polymorphic Modifications of Pm2O3. J Am Ceram Soc 1972;55:428.

[51] Heung LK. Titanium for long-term tritium storage. 1994.

[52] Olsen LC, Cabauy P, Elkind BJ. Betavoltaic power sources. Phys Today 2012;65:35.

[53] Bartlit JR, Denton WH, Sherman RH. hydrogen isotope distillation for the Tritium Systems Test Assembly. 1978.

[54] Furukawa S, Mehregany M. Electroless plating of nickel on silicon for fabrication of high-aspect-ratio microstructures. Sensors Actuators A Phys 1996;56:261–6.

[55] Hinderer JH. Radioisotopic impurities in promethium-147 produced at the ORNL high flux isotope reactor 2010.

[56] Oh K, Prelas MA, Rothenberger JB, Lukosi ED, Jeong J, Montenegro DE, et al. Theoretical maximum efficiencies of optimized slab and spherical betavoltaic systems utilizing Sulfur-35, Strontium-90, and Yttrium-90. Nucl Technol 2012;179:234–42.

[57] Revankar ST, Adams TE. Advances in betavoltaic power sources. J Energy Power Sources 2014;1:321–9.

[58] Wacharasindhu T, Kwon JW, Meier DE, Robertson JD. Liquid-semiconductor-based micro power source using radioisotope energy conversion. Solid-State Sensors, Actuators Microsystems Conf. 2009. TRANSDUCERS 2009. Int., 2009, p. 656–9.

[59] Kim B, Sharbono C, Ritzdorf T, Schmauch D. Factors affecting copper filling process within high aspect ratio deep vias for 3D chip stacking. Electron. Components Technol. Conf. 2006. Proceedings. 56th, 2006, p. 6--pp.

[60] Bellinger SL, Cooper BW, Fronk RG, Henson LC, Ochs TR, Sobering TJ, et al. Characterization of microstructured semiconductor neutron detectors. IEEE Nucl. Sci. Symp, 2013, p. 1–7.